CSIRO PUBLISHING www.publish.csiro.au/journals/eg Copublished paper, please cite all three:
Exploration Geophysics, 2008, **39**, 41–51; *Butsuri-Tansa*, 2008, **61**, 41–51; *Mulli-Tamsa*, 2008, **11**, 41–51

Velocity-porosity relationships in oceanic basalt from eastern flank of the Juan de Fuca Ridge: The effect of crack closure on seismic velocity

Takeshi Tsuji[1,3] Gerardo J. Iturrino[2]

[1]Department of Civil and Earth Resources Engineering, Kyoto University, Katsura Campus, Nishikyo-ku, Kyoto 615-8540, Japan.
[2]Lamont-Doherty Earth Observatory of Columbia University, P.O. Box 1000, 61 Route 9W Palisades, NY 10964-1000, USA.
[3]Corresponding author. Email: tsuji@earth.kumst.kyoto-u.ac.jp

Abstract. To construct in situ velocity-porosity relationships for oceanic basalt, considering crack features, P- and S-wave velocity measurements on basaltic samples obtained from the eastern flank of the Juan de Fuca Ridge were carried out under confining pressures up to 40 MPa. Assuming that the changes in velocities with confining pressures are originated by micro-crack closure, we estimated micro-crack aspect ratio spectra using the Kuster-Toksöz theory. The result demonstrates that the normalised aspect ratio spectra of the different samples have similar characteristics. From the normalised aspect ratio spectrum, we then constructed theoretical velocity-porosity relationships by calculating an aspect ratio spectrum for each porosity. In addition, by considering micro-crack closure due to confining pressure, a velocity-porosity relationship as a function of confining pressure could be obtained. The theoretical relationships that take into account the aspect ratio spectra are consistent with the observed relationships for over 100 discrete samples measured at atmospheric pressure, and the commonly observed pressure dependent relationships for a wide porosity range. The agreement between the laboratory-derived data and theoretically estimated values demonstrates that the velocity-porosity relationships of the basaltic samples obtained from the eastern flank of the Juan de Fuca Ridge, and their pressure dependence, can be described by the crack features (i.e. normalised aspect ratio spectra) and crack closure.

Key words: velocity-porosity relationship, oceanic basalt, crack aspect ratio, Kuster-Toksöz theory, and Integrated Ocean Drilling Program.

Introduction

Relationships between velocity and porosity for the in-situ oceanic basalt layer have not been adequately established because velocities are highly dependent on effective pressure due to thin crack closure. It has been previously established that velocities of basalts are significantly influenced by crack geometry as well as crack aspect ratios (e.g. Wilkens et al., 1988; Wilkens et al., 1991; Ludwig et al., 1998; Cerney and Carlson, 1999). Therefore, to construct a relationship between velocity and porosity, we need to consider changes in crack aspect ratio and crack closure with effective pressure. In addition, when constructing a velocity-porosity relationship, it is equally important to evaluate the degree and type of alteration as well as fracture characteristics, because hydrothermal alteration and the formation of secondary minerals significantly influence the crack features of the oceanic crust (Alt et al., 1986; Cerney and Carlson, 1999).

Here, we first present the results of P- and S-wave velocity measurements that were made on basaltic samples obtained from Expedition 301 of the Integrated Ocean Drilling Program (IODP) as a function of confining pressure, and then apply the Kuster-Toksöz theory (Kuster and Toksöz, 1974) to investigate crack features (crack aspect ratio spectrum). From these features we subsequently attempt to construct theoretical velocity-porosity relationships as a function of confining pressure. To check the accuracy of the calculated relations, furthermore, we measured over 100 discrete samples at atmospheric pressure.

Geologic setting

Site U1301 (Figure 1) is located on a buried basement ridge (Second Ridge) of 3.6 Ma old crust. It is 100 km east of the crest of the Juan de Fuca Ridge that has been spreading at a rate of ∼3 cm/yr (Davis and Currie, 1993). The basement relief in this area is generally characterised by linear ridges and troughs sub-parallel to the spreading centre, which have been mainly produced by faulting, variation of magmatic supply at the ridge, and off-axis volcanism. Although low-permeability sediments cover the basement and limit heat loss across most of the ridge flank, Fisher et al. (1997) demonstrated that the pore pressure within the oceanic crust was close to hydrostatic near the drilling site. During previous drilling activities in this area (Fisher and Davis, 2000), core samples and downhole logging data were acquired within the sedimentary section and sediment-basement interface. However Hole U1301B is the first borehole to investigate several hundred metres of the topmost oceanic crust in this area (Fisher et al., 2005).

During IODP Expedition 301, three holes (U1301A, U1301B, and U1301C) were drilled at this site. The seafloor depth at the drilling site is 2667 m below sea surface. Crustal samples were recovered from 351 to 583 m below seafloor (mbsf) or 86 to 318 m below the sediment-basement interface. The core recovery in this interval is ∼30% and the lithostratigraphic sequences consist of pillow basalt, massive basalt, and basalt-hyaloclastite. We will discuss the properties of the basaltic samples from Hole U1301B in the next section.

 10.1071/EG08001 0812-3985/08/010041

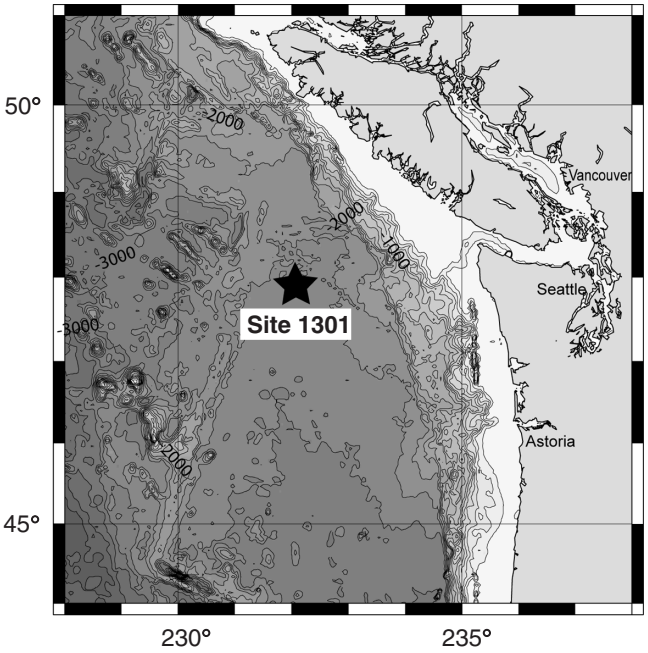

Fig. 1. Bathymetric map of the eastern flank of the Juan de Fuca plate. Black star represents the location of IODP Site U1301.

Experimental procedures and results

Sample description and classification

Pillow basalts are the most abundant lithology recovered from Hole U1301B and are identified by the presence of curved chilled margins, oblique to the vertical axis of the core, with perpendicular radial cooling cracks. They are subdivided into aphyric and sparsely to moderately phyric basalts, based on phenocryst mineralogy and relative abundances (Expedition 301 Scientists, 2005). Core intervals, composed of sparsely to moderately plagioclase + clinopyroxene ± olivine basalts, tend to have glassy to microcrystalline textures. Using mineral maps obtained with an Electron Probe Micro-Analyzer (Tsuji and Yamaguchi, 2007), pillow basalts used for this study were divided into (1) pillow margins and (2) central part of pillow lava. Samples of massive basalts (sparsely plagioclase + clinopyroxene ± olivine basalts) were generally characterised by grain size variations grading from glassy to fine-grained textures towards the centre of the flows.

Velocities and index properties were measured on 10 oriented minicores with the following distribution: (1) four samples were cut from the pillow margins, (2) three samples from centre part of pillow lavas, and (3) three samples from massive flow sections (Table 1). The samples were obtained from the IODP whole round cores (Figure 2*a*) with the minicore principal axis corresponding to the vertical direction (*z*-axis), and we measured velocities in the vertical direction (*z*-axis). The dimensions of the minicores are 2.54 cm (1 inch) in diameter and ~4.5 cm in length. The ends of the minicores were polished to be flat and parallel in order to ensure good coupling with the transducers while performing high-pressure velocity experiments.

In addition to minicore measurements, we measured physical properties on over 100 cubic samples at atmospheric pressure and surface temperature conditions during the IODP Expedition 301 (small dots in Figure 3). The cubic samples are ~2.1 cm on each side and P-wave velocities were measured in three orthogonal directions (Figure 2*b*).

Index properties

Density and porosity values were obtained from saturated and dry weights, and dry volumes. Saturated minicore samples were immersed in seawater and placed in a vacuum for 24 h whereas dry minicore samples were obtained by drying them for 24 h at 100°C. Minicore bulk densities range from 2.69 to 2.90 t/m^3, grain densities from 2.78 to 2.93 t/m^3, and porosities from 1.27 to 4.84% with an average value of 2.58% (Table 1, Figure 3). The average minicore porosity value is lower than that of cubic samples (~5.47%) because the latter could be obtained from the portions with high-porosity intervals with high-fracture densities (black dots in Figure 3). There is no significant trend in index properties as a function of depth (Figure 3) although properties of cubic samples seem to change locally due to variations in degrees of alteration and fracturing. These variations seem to correspond to well defined boundaries such as the location of pillow lava units and the boundaries between pillow lavas and massive units (Expedition 301 Scientists, 2005).

P- and S-wave velocities

We used the pulse transmission technique (Birch, 1960) to determine P- and S-wave velocities under applied confining pressures. Minicores were jacketed with rubber tubing to isolate them from the confining pressure medium. A high-viscosity adhesive was used to bond the transducers to the minicores. The principal frequencies used were 1 MHz and 500 kHz for P- and S-wave velocity measurements, respectively. The experimental configuration allowed simultaneous measurement of P- and S-wave travel-times at confining pressures ranging from 1.4 MPa (200 psi) to 40 MPa (5800 psi) (Figure 4). Although we wanted to measure velocities up to ~150 MPa in order to consider closure of relatively thick cracks, we could not measure them under such a high confining pressure due to limitation of our pressure vessel. Travel-times were measured after digitising each trace with 1000 points over a time sweep of $\sim 2 \times 10^{-5}$ s, with a resulting time resolution of $\sim 2 \times 10^{-8}$ s. The recorded waveforms (Figure 4) demonstrate change in travel time and amplitude with confining pressure. We could easily determine the first arrival of waveforms, except for S-wave at low confining pressure (Figure 4). From the amplitude variation for each frequency component, furthermore, we can evaluate attenuation (see Appendix).

P- and S-wave travel-times of minicores were first measured under dry conditions (Figure 5) and then pore fluid pressure was applied to obtain saturated-condition measurements. However, we could not effectively measure travel-times under saturated conditions in this way, because the sample permeabilities were significantly low. Instead, the minicores were saturated within a separate vessel, under vacuum for 24 h, and the saturated velocities were measured (Figure 5). Therefore, in both dry and saturated conditions, pore pressures correspond to atmospheric pressure, and the effective pressures (or differential pressure) correspond to confining pressures when fluid-matrix interaction (e.g. Biot, 1955) is ignored.

The dry P-wave velocities at a confining pressure of 40 MPa range from 5135 m/s to 6234 m/s, with an average value of 5727 m/s (Table 1, Figure 5). S-wave velocities under the same conditions range from 3025 m/s to 3580 m/s, with an average value of 3328 m/s. The velocities in pillow centres (Figures 5*b* and 5*e*) are higher than those in pillow margins (Figures 5*a* and 5*d*). The P-wave velocities under dry and saturated conditions are similar, except for results from a high-porosity sample (32R-2W). P-wave velocity under saturated conditions should be faster than that under dry conditions because the rock elastic bulk modulus usually stiffens when air in dry pores is

Table 1. Bulk densities, grain densities, porosities, and P- and S-wave velocities of minicore samples recovered from the eastern flank of the Juan de Fuca Ridge. Velocity values were obtained as a function of effective pressure.

Sample name Section, Interval Depth	Bulk density (t/m^3)	Grain density (t/m^3)	Porosity (%)		Velocity (km/s) – Effective pressure (MPa) 1.4	2.8	4.1	5.5	9.0	12.4	15.9	19.3	22.8	26.2	29.7	33.1	36.6	40.0
2R-3W 142–147				Vp, dry	5.44	5.45	5.47	5.47	5.48	5.49	5.49	5.51	5.51	5.51	5.52	5.52	5.52	5.52
361.46 mbsf	2.78	2.85	3.72	Vs, dry							3.00	3.04	3.05	3.08	3.09	3.12	3.14	3.16
Pillow margin				Vp, sat	5.39	5.41	5.42	5.43	5.44	5.45	5.46	5.47	5.48	5.49	5.49	5.50	5.51	5.52
				Vs, sat					2.96	3.01	3.02	3.06	3.08	3.09	3.10	3.12	3.12	3.12
4R-3W 123–128				Vp, dry	5.43	5.47	5.48	5.49	5.50	5.52	5.53	5.54	5.54	5.54	5.54	5.54	5.54	5.55
370.62 mbsf	2.85	2.90	2.85	Vs, dry			3.06	3.09	3.10	3.10	3.11	3.13	3.16	3.17	3.19	3.22	3.22	3.23
Pillow margin				Vp, sat		5.49	5.50	5.50	5.51	5.52	5.53	5.54	5.54	5.55	5.56	5.56	5.57	5.57
				Vs, sat		3.04	3.05	3.07	3.09	3.11	3.12	3.13	3.14	3.14	3.15	3.16	3.16	3.17
11R-1W 80–85				Vp, dry		5.40	5.42	5.44	5.45	5.46	5.47	5.47	5.47	5.49	5.49	5.49	5.49	5.49
425.20 mbsf	2.79	2.86	3.44	Vs, dry			3.09	3.12	3.14	3.14	3.15	3.16	3.17	3.23	3.26	3.29	3.29	3.29
Massive				Vp, sat			5.40	5.41	5.42	5.43	5.44	5.44	5.44	5.44	5.44	5.44	5.44	5.44
				Vs, sat			3.19	3.21	3.22	3.23	3.23	3.24	3.25	3.26	3.27	3.27	3.27	3.28
15R-3W 66–71				Vp, dry	5.79	5.81	5.81	5.82	5.83	5.85	5.87	5.87	5.87	5.87	5.87	5.87	5.89	5.89
447.26 mbsf	2.88	2.91	1.70	Vs, dry			3.34	3.37	3.37	3.37	3.38	3.39	3.39	3.39	3.40	3.40	3.41	3.41
Massive				Vp, sat	5.76	5.77	5.77	5.78	5.78	5.79	5.81	5.81	5.81	5.83	5.83	5.85	5.85	5.86
				Vs, sat		3.35	3.36	3.36	3.37	3.37	3.38	3.39	3.39	3.39	3.40	3.40	3.40	3.41
18R-2W 16–21				Vp, dry	5.51	5.52	5.52	5.52	5.53	5.55	5.55	5.56	5.56	5.58	5.58	5.58	5.58	5.58
472.46 mbsf	2.84	2.89	2.50	Vs, dry		3.18	3.19	3.21	3.22	3.22	3.23	3.23	3.24	3.25	3.25	3.26	3.26	3.26
Massive				Vp, sat		5.54	5.55	5.55	5.56	5.56	5.57	5.58	5.58	5.58	5.58	5.58	5.59	5.59
				Vs, sat		3.17	3.19	3.20	3.21	3.22	3.23	3.25	3.26	3.26	3.26	3.27	3.27	3.27
21R-4W 62–67				Vp, dry		6.02	6.03	6.03	6.05	6.07	6.08	6.08	6.09	6.10	6.11	6.11	6.11	6.11
495.11 mbsf	2.89	2.93	2.05	Vs, dry		3.38	3.39	3.42	3.43	3.43	3.43	3.44	3.45	3.46	3.46	3.48	3.48	3.48
Pillow centre				Vp, sat		6.02	6.03	6.04	6.06	6.08	6.09	6.10	6.10	6.11	6.11	6.12	6.13	6.13
				Vs, sat		3.35	3.36	3.37	3.39	3.40	3.41	3.43	3.44	3.46	3.47	3.48	3.48	3.48
24R-1W 102–107				Vp, dry	5.64	5.66	5.67	5.68	5.69	5.71	5.72	5.75	5.75	5.75	5.75	5.75	5.76	5.76
506.92 mbsf	2.80	2.84	1.85	Vs, dry	3.03	3.09	3.17	3.22	3.26	3.28	3.30	3.31	3.31	3.33	3.33	3.35	3.35	3.36
Pillow margin				Vp, sat		5.67	5.68	5.69	5.69	5.70	5.71	5.71	5.72	5.73	5.74	5.75	5.75	5.76
				Vs, sat			3.26	3.27	3.28	3.31	3.34	3.35	3.36	3.37	3.37	3.37	3.38	3.38
25R-1W 8–13				Vp, dry	6.15	6.18	6.18	6.19	6.20	6.21	6.22	6.22	6.23	6.23	6.23	6.23	6.23	6.24
509.58 mbsf	2.90	2.93	1.54	Vs, dry		3.46	3.49	3.50	3.52	3.54	3.54	3.55	3.56	3.57	3.58	3.58	3.58	3.58
Pillow centre				Vp, sat		6.16	6.18	6.19	6.20	6.21	6.22	6.22	6.23	6.23	6.24	6.24	6.24	6.24
				Vs, sat		3.48	3.53	3.55	3.57	3.58	3.58	3.58	3.58	3.59	3.59	3.60	3.60	3.60
32R-2W 44–49				Vp, dry	5.03	5.05	5.05	5.05	5.07	5.08	5.09	5.10	5.11	5.12	5.12	5.13	5.13	5.14
551.88 mbsf	2.69	2.78	4.84	Vs, dry		2.89	2.91	2.93	2.96	2.97	2.98	2.99	3.01	3.02	3.03	3.03	3.03	3.03
Pillow margin				Vp, sat		5.16	5.17	5.18	5.19	5.19	5.20	5.21	5.21	5.22	5.23	5.24	5.24	5.25
				Vs, sat				2.92	2.94	2.95	2.96	2.97	2.98	2.98	2.99	3.00	3.00	3.00
35R-2W 133–138				Vp, dry		5.95	5.96	5.97	5.98	5.99	6.00	6.01	6.02	6.02	6.03	6.04	6.04	6.04
566.4 mbsf	2.90	2.93	1.27	Vs, dry		3.44	3.45	3.46	3.46	3.47	3.47	3.47	3.47	3.48	3.48	3.48	3.48	3.48
Pillow centre				Vp, sat		5.99	6.00	6.00	6.01	6.02	6.03	6.03	6.04	6.04	6.05	6.06	6.06	6.06
				Vs, sat			3.46	3.47	3.48	3.48	3.48	3.49	3.49	3.49	3.49	3.50	3.50	3.51

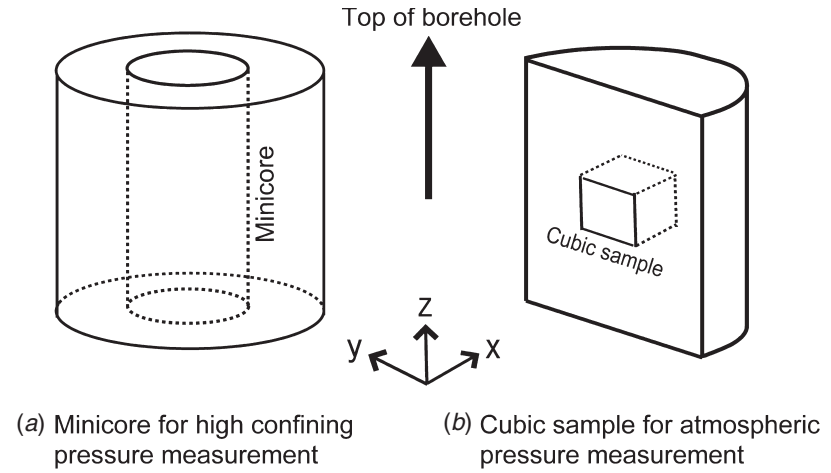

Fig. 2. (*a*) Schematic image showing the orientation of minicores extracted from whole round cores. Ten minicores were used for high pressure experiments. (*b*) Schematic of cubic samples extracted from the working half of the split core (Expedition 301 Scientists, 2005). The cubic samples are ~2.1 cm on each side. More than 100 cubic samples were used for atmospheric pressure experiments. Measured velocities on cubic samples were obtained in three orthogonal directions (*x*, *y*, *z*-axes).

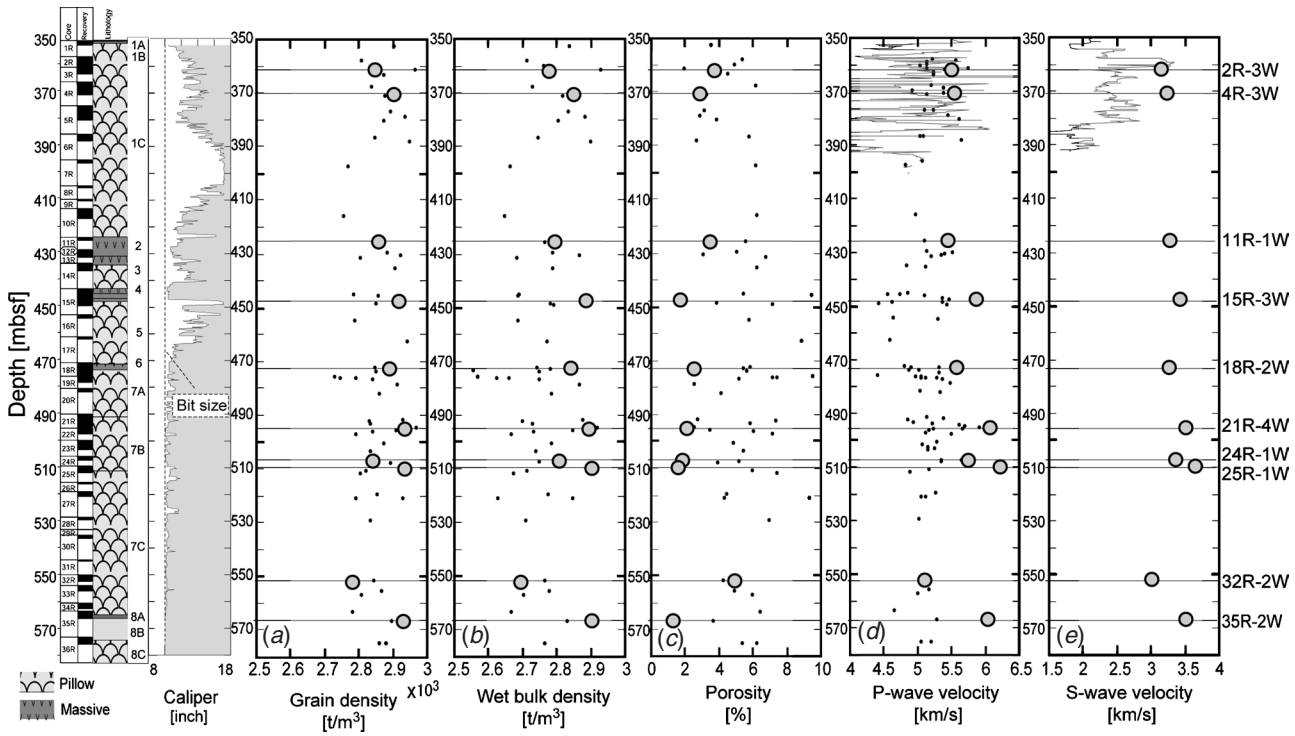

Fig. 3. Depth profiles of (*a*) grain density, (*b*) bulk density, (*c*) porosity, (*d*) P-wave velocity, and (*e*) S-wave velocity. Large dots represent the results of minicore measurements. Minicore velocity values used in this figure were obtained at a confining pressure of 40 MPa in dry conditions. Small dots represent the results of cubic samples measured at atmospheric pressure (Expedition 301 Scientists, 2005). Curves in the profiles of P- and S-wave velocities represent downhole logging data.

replaced with less-compressible seawater (e.g. Toksöz et al., 1976). One of the explanations for similar velocities between dry and saturated conditions is that the samples may not have been totally saturated, because P-wave velocities are much increased near totally saturated conditions (Knight and Nolen-Hoeksema, 1990).

The P- and S-wave velocities obtained from logging data (lines in Figure 3) show more scatter and are slower than those obtained from laboratory measurements (dots in Figure 3). There are inherent difficulties in comparing high frequency laboratory data with low frequency logging data, because of dispersion. Furthermore, the difference in velocities could arise from the different spatial scales measured by different measurement techniques; for example, fracture porosity occurring at a scale larger than the laboratory samples can only be detected by logging measurements.

At low confining pressure, both P- and S-wave velocities increase rapidly with confining pressures (Figure 5), primarily due to closure of micro-cracks and flaws (e.g. Kuster and Toksöz, 1974). This velocity increase is important, because we can estimate the crack aspect ratio spectrum from the change in velocity with confining pressure.

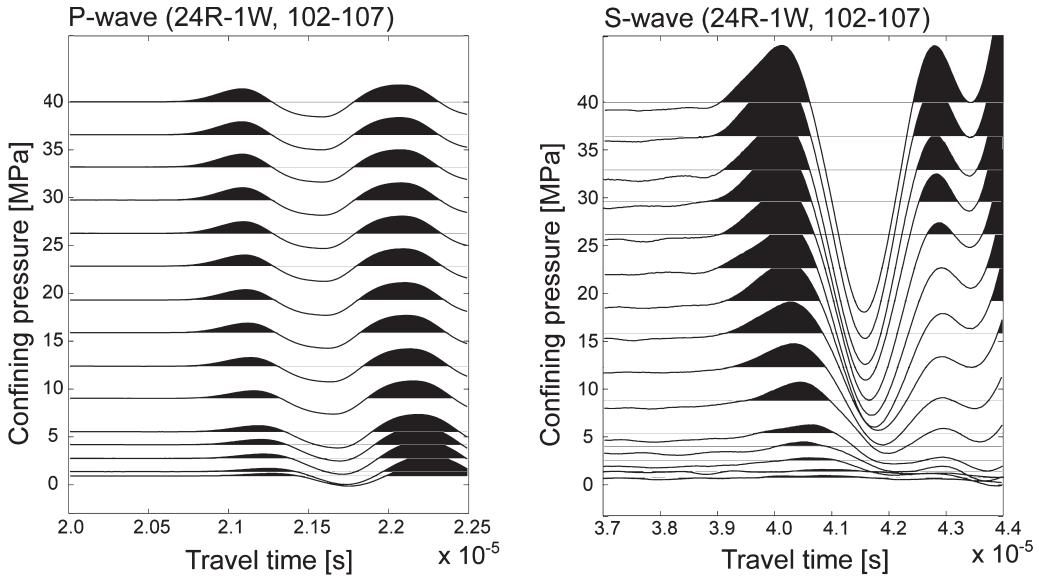

Fig. 4. Recorded waveform at each confining pressure. These waveforms were recorded in dry conditions. Vertical axis represents confining pressure, and horizontal axis represents time in seconds.

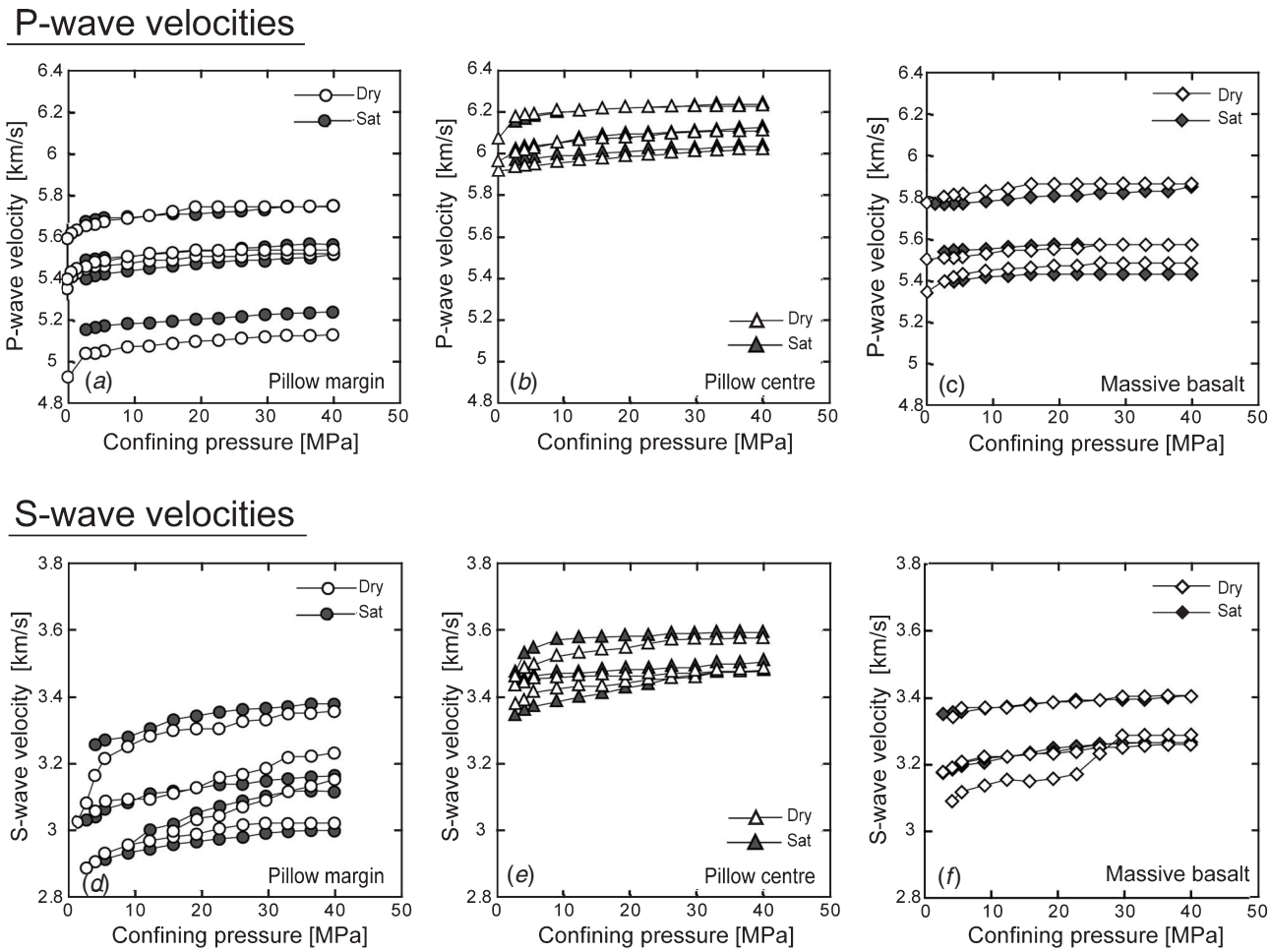

Fig. 5. Plots representing P-wave velocities measured as a function of confining pressure in samples from (*a*) the pillow margins, (*b*) the centre parts of pillow basalts, and (*c*) massive basalts. S-wave velocities as a function of confining pressure in (*d*) the pillow margins, (*e*) the centre parts of pillow basalts, and (*f*) the massive basalts. Open and solid symbols represent velocities in dry and saturated conditions, respectively.

Discussion

Micro-crack aspect ratio spectrum

Seismic velocities of consolidated rock (e.g. basalt) vary with confining pressure (Figure 5) mainly due to crack closure in the rock (e.g. Kuster and Toksöz, 1974), so the pore space of our basaltic samples can be modelled as cracks. Because the change in velocity with confining pressure is a measure of the amount of micro-crack closure at a particular pressure (e.g. Toksöz et al., 1976), micro-crack aspect ratio spectra can be estimated from the

relationship between velocity and confining pressure. Although the cracks in our minicore samples mainly originated as a result of degassing, fracturing and alteration, some were also induced by drilling operations and expansion due to pressure release. Since we cannot distinguish the origins of cracks, we estimate the aspect ratio spectrum over the wide variety of micro-cracks.

In this application, a 'pore' is considered to be a randomly oriented ellipsoidal crack, which can be described by its aspect ratio. Furthermore, the pore space in a rock is assumed to be made up of pores with various aspect ratios. Kuster and Toksöz (1974) derived expressions for P- and S-wave velocities by using a long-wavelength first-order scattering theory. For a two-phase material, the effective elastic moduli (K_n^* and μ_n^*) at a confining pressure P_n can be calculated by the following expressions:

$$\frac{K_n^* - K}{K' - K}\frac{3K + 4\mu}{3K_n^* + 4\mu} = \sum_{m=1}^{M} \alpha_m \left[1 + \frac{dc}{c}(\alpha_m, P_n)\right] \frac{1}{3} T_{iijj}(\alpha_{mn}) \frac{c(\alpha_m)}{\alpha_m}, \quad (1)$$

and

$$\frac{\mu_n^* - \mu}{\mu' - \mu}\frac{25\mu(3K + 4\mu)}{6\mu_n^*(K + 2\mu) + \mu(9K + 8\mu)} = \sum_{m=1}^{M} \alpha_m \left[1 + \frac{dc}{c}(\alpha_m, P_n)\right]\left[T_{ijij}(\alpha_{mn}) - \frac{1}{3} T_{iijj}(\alpha_{mn})\right] \frac{c(\alpha_m)}{\alpha_m}, \quad (2)$$

where K and μ are the grain elastic moduli; K' and μ' are the inclusion moduli; α_m and $c(\alpha_m)$ are the m-th aspect ratio and its corresponding concentration; and $T_{iijj}(\alpha_{mn})$ and $T_{ijij}(\alpha_{mn})$ are scalar quantities calculated for an oblate spheroid pore as a function of aspect ratio, taking into account the pore shape and elastic properties (Kuster and Toksöz, 1974; Mavko et al., 1998). The term $dc(\alpha_m, P_n)$ is the fractional change in the concentration of aspect ratio α_m of an ellipsoidal pore at a confining pressure P_n (Toksöz et al., 1976; Cheng and Toksöz, 1979) that can be described as:

$$\frac{dc(\alpha_m, P_n)}{c(\alpha_m)} = \frac{-P_n}{K_A^*} \Big/ \left[E_1 - E_2 E_3/(E_3 + E_4)\right], \quad (3)$$

where E_i are functions of aspect ratio α and some effective matrix moduli defined as the effective static matrix moduli of the rock with all the pores except those with aspect ratio α (Toksöz et al., 1976). The term K_A^* is the static bulk modulus of the empty rock (Toksöz et al., 1976). Because the static bulk modulus is unknown, it is taken to be the dynamic bulk modulus of the dry rock (Cheng and Toksöz, 1979). When dc/c (equation 3) is less than -1, we consider that the cracks of aspect ratio α_m are closed. Because the Kuster-Toksöz theory neglects any crack-crack interactions, it becomes invalid as the total number of cracks grows large because the no crack interaction assumption is violated. However, in low-porosity basaltic samples such as those measured in this study ($\sum_i \frac{c(\alpha_i)}{\alpha_i} < 1$), the theory provides reasonable estimates.

We estimated the concentration of aspect ratios $c(\alpha_m)/\alpha_m$ and grain elastic moduli with equations (1) and (2) using inversion techniques (Cheng and Toksöz, 1979; Ludwig et al., 1998; Cerney and Carlson, 1999). The initial choice of aspect ratios for the inversion is arbitrary, so the aspect ratio spectrum obtained by inverting the velocity data is not unique but depends on the initial choice of aspect ratios. In this study, a total of seven different aspect ratios (0.1, 0.01, 0.000562, 0.000316, 0.000178, 0.0001, and 0.0000562) were used. The lower aspect ratio distribution (from 0.000562 to 0.0000562) was chosen so that each aspect ratio is effectively closed at successive pressure increments (Cerney and Carlson, 1999). However, we could not estimate an accurate concentration of crack aspect ratios over ~0.000562 because the larger crack aspect ratios do not close up at the maximum confining pressures of 40 MPa, because of the stiffness of the basaltic samples. Furthermore, bulk moduli of some basaltic samples are not much changed with confining pressure, and the trends are different from the theoretically estimated value. Therefore, we ignored the highly anomalous parts for inversion.

Inversion results demonstrate that aspect ratio spectra $c(\alpha)$ for the different samples have similar characteristics (Figure 6*a*). We could not find a significant difference in aspect ratio spectra between pillow basalts and massive basalts, although the grain elastic moduli are different for each sample. By summing the concentration of cracks of various aspect ratios (Figure 6*a*), the total porosity $\phi = \sum_i c(\alpha_i)$ can be obtained.

Relation between velocity and porosity

Examining the velocity-porosity relationships, we find that P- and S-wave velocities clearly decrease with increasing porosity (Figure 7), as seen in previous studies such as those from Hole 504B (Wilkens et al., 1983) and Hole s896A (Wilkens and

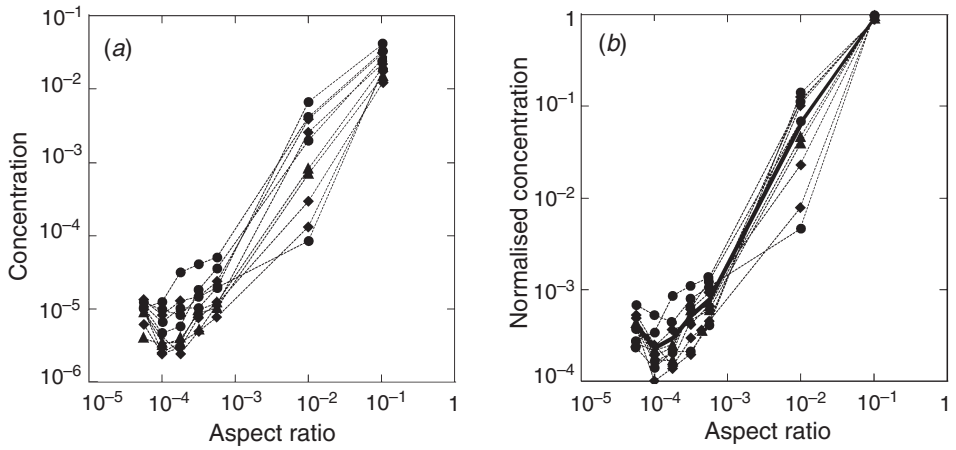

Fig. 6. (*a*) Aspect ratio spectra $c(\alpha_m)$ estimated from relationships between velocities and confining pressures (Figure 5). Vertical axis represents concentration of each aspect ratio on a logarithmic scale. Horizontal axis represents aspect ratio on a logarithmic scale. The sum of all concentration values corresponds to the total porosity. (*b*) Normalised aspect ratio spectra $c_{nor}(\alpha_m)$. Vertical axis represents normalised concentration of each aspect ratio on a logarithmic scale. Horizontal axis represents aspect ratio on a logarithmic scale. The sum of all normalised concentration values equals one. Bold line represents the averaged normalised aspect ratio spectrum $c_{ave}(\alpha_m)$.

Salisbury, 1996). Although the P-wave velocities measured in low-porosity samples are similar to those recovered from Holes U1301B, 504B, and 896A, the velocities measured in high-porosity (>5%) samples from Hole U1301B are lower than those from Holes 504B and 896A.

The theoretical relationships derived using the Kuster-Toksöz theory, assuming a constant crack aspect ratio α (e.g. Wilkens et al., 1991), demonstrate that the average pore aspect ratio of samples from Hole U1301B is between 0.05 and 0.1 (Figure 7), and minicore samples from Hole U1301B seem to be influenced by lower crack aspect ratios more than those from Holes 504B and 896A. However, this estimate ($\alpha = 0.05 - 0.1$) assumes that all pore spaces have the same aspect ratio α, which is highly unrealistic because, as shown in Figure 6*a*, pore spaces can have a wide range of aspect ratios. In addition, velocities are significantly increased by crack closure under confining pressures (Figure 5). Therefore, the velocity-porosity relationship should take into account the effect of confining pressure.

Accordingly, we derive a theoretical relation between velocities and porosities as a function of confining pressures, using aspect ratio spectra $c(\alpha_m)$ (Figure 6*a*). First, the aspect ratio spectrum is normalised by total porosity $\phi = \sum_i c(\alpha_i)$ for each sample (Figure 6*b*) (Cerney and Carlson, 1999):

$$c_{nor}(\alpha_m) = c(\alpha_m)/\phi. \quad (4)$$

The sum of the normalised concentrations (equation 4) becomes one, and the porosity is a scaling factor. The normalised concentrations of all samples are then averaged (bold line in Figure 6*b*) (Cerney and Carlson, 1999), as follows:

$$c_{ave}(\alpha_m) = \sum_j c^j_{nor}(\alpha_m)/N, \quad (5)$$

where j is a sample index, and N denotes the number of samples. This averaged normalised concentration represents the characteristics of pore space of all the minicore samples. In order to match total aspect ratio concentration, the averaged normalised concentration (equation 5) is multiplied by a porosity term, $c_{ave}(\alpha_m) \cdot \phi$, and this allows the calculation of the effective elastic moduli (K^*, μ^*) for a wide porosity range by entering $c_{ave}(\alpha_m) \cdot \phi$ and the averaged grain elastic moduli ($K_{ave} = 62.8$, $\mu_{ave} = 34.4$) into the Kuster-Toksöz equation. In this analysis, we assume that the average normalised concentration of aspect ratios (eqn 5) is similar over a wide porosity range. Similar Poisson's ratio for minicore samples (Figure 8) demonstrates

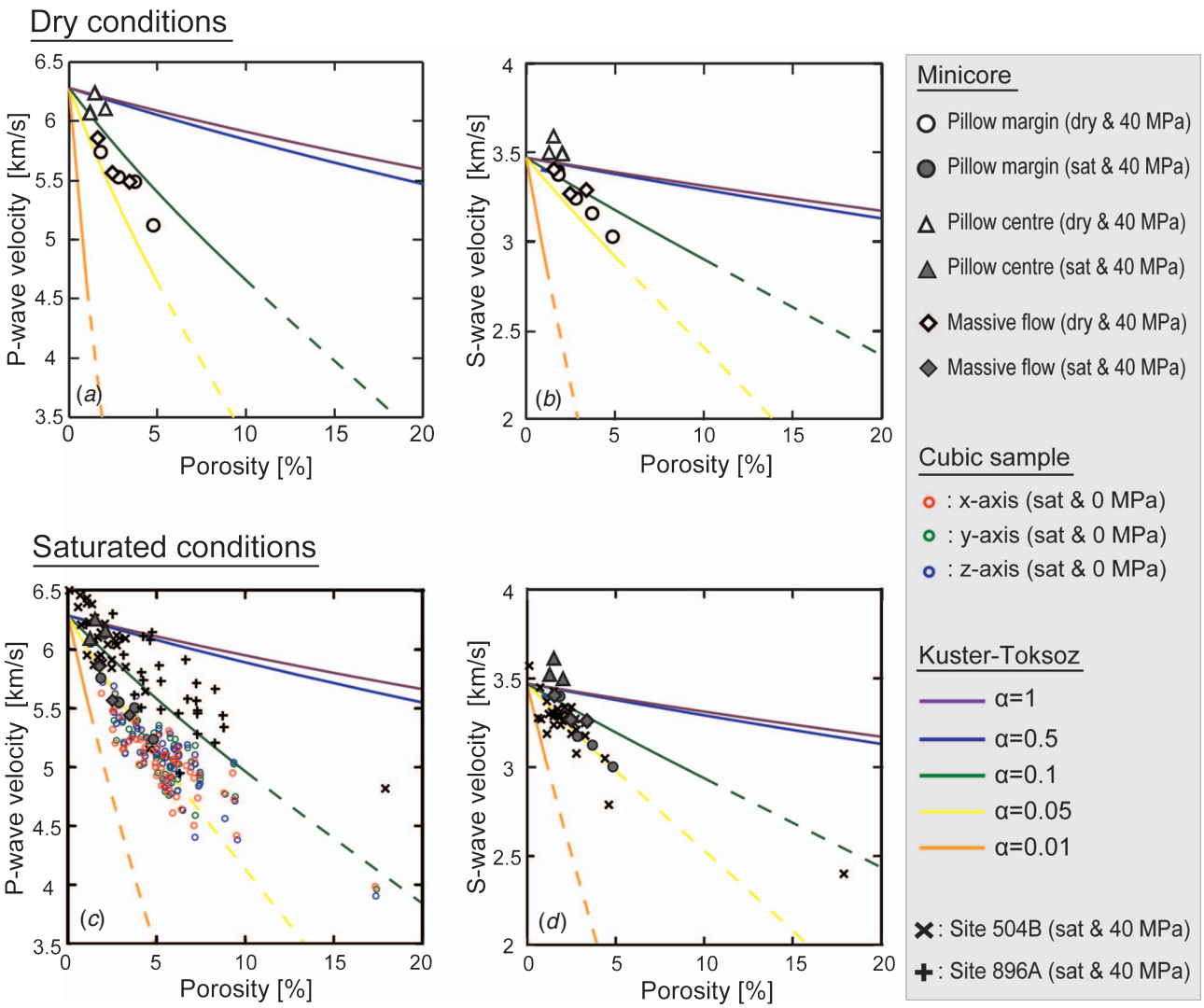

Fig. 7. Diagrams showing velocity-porosity relationships in conjunction with relationships for constant aspect ratio (lines) obtained using the Kuster-Toksöz theory. Open and solid symbols represent minicore measurements in dry and saturated conditions, respectively. Red, green, and blue dots represent cubic sample measurements at atmospheric pressure for *x*, *y*, and *z* directions, respectively. The relationship obtained from the discrete samples from Holes 504B and 896A is also presented (*Wilkens et al., 1983; Wilkens and Salisbury, 1996). The dashed sections indicate regions beyond the constraint proposed by Kuster and Toksöz (1974).

that the crack aspect ratio spectra for the different samples have similar characteristics, because the introduction of different aspect crack ratios into a host rock generally affects P- and S-wave velocities differently and so changes Poisson's ratio (e.g. Hyndman, 1979; Shearer, 1988; Swift et al., 1998).

The results show that the theoretical velocity-porosity relationship calculated from the aspect ratio spectrum (black line in Figure 9) is consistent with our laboratory-derived data including our cubic samples obtained at atmospheric pressure (coloured dots in Figure 9*a*). The agreement of the theoretical relationship with laboratory data for a wide porosity range demonstrates that the velocity-porosity relationship is primarily dependent on crack features; basaltic samples over a wide porosity range have similar normalised aspect ratio spectra. Furthermore, the velocity-porosity relationship as a function of confining pressures (coloured lines in Figure 9) can be calculated from the averaged normalised aspect ratio spectrum, by considering crack closure to be caused by the increase in confining pressure (eqn 3). From these relationships, we calculated velocities at in situ effective pressures, and velocity differences between in situ effective pressure and atmospheric pressure conditions.

Although we could not estimate an accurate concentration of aspect ratios over ~0.000562 from our experimental pressure ranges, lower aspect ratio cracks have a greater effect on the velocity-porosity relation (Kuster and Toksöz, 1974). Furthermore, the Kuster-Toksöz theory does not take into account crack-to-crack interactions and the approximation is only valid for low concentrations of cracks. Porosities higher than ~5% lie beyond the Kuster-Toksöz constraint $\sum_i \frac{c(\alpha_i)}{\alpha_i} < 1$ (dashed lines in Figures 7, 8, and 9) although some studies have demonstrated that the strict constraints are not necessary for small aspect ratio and low porosity samples (Berryman, 1980; Berryman and Berge, 1996). In our case, the relationship considering aspect ratio spectrum is consistent with high porosity (~10%) samples regardless of the Kuster-Toksöz constraint.

Conclusion

P- and S-wave velocities of basaltic samples from the eastern flank of the Juan de Fuca Ridge were measured under confining pressures. From the relationships between velocity and confining pressure, we estimated the micro-crack aspect ratio spectra using the Kuster-Toksöz theory. Further, considering the aspect ratio

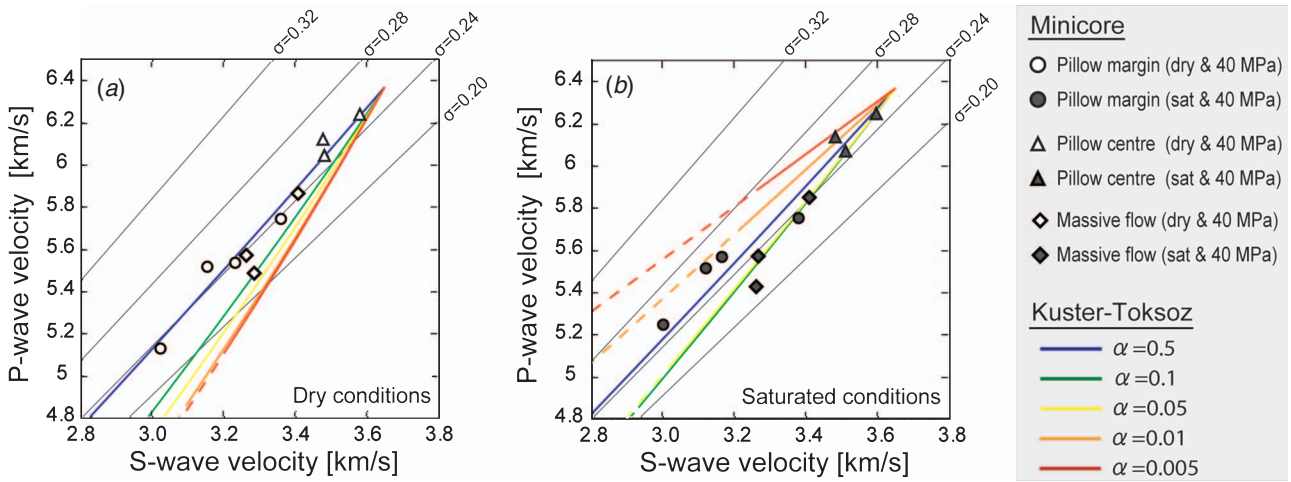

Fig. 8. P- and S-wave velocity cross plot in (*a*) dry conditions and (*b*) saturated conditions. Constant Poisson's ratios are represented in black lines. Relationships as a function of constant aspect ratio obtained using the Kuster-Toksöz theory are represented by coloured lines. The dashed sections indicate regions beyond the constraint proposed by Kuster and Toksöz (1974).

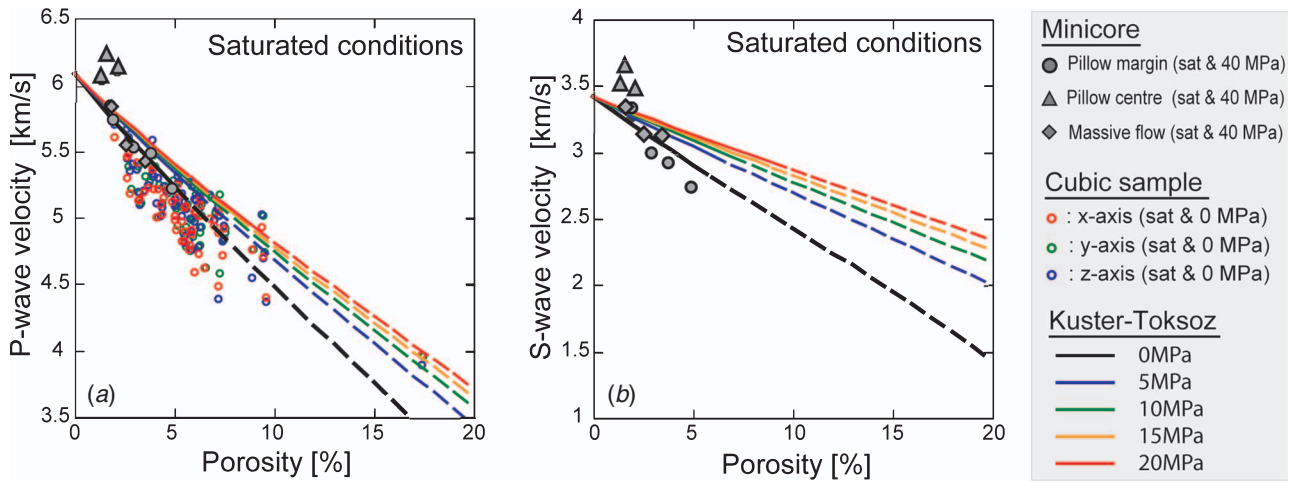

Fig. 9. (*a*) The relationships between P-wave velocity and porosity as a function of confining pressure (lines) obtained using the Kuster-Toksöz theory. (*b*) The relationships between S-wave velocity and porosity as a function of confining pressure (lines) obtained using the Kuster-Toksöz theory. Solid symbols represent minicore measurements obtained at a confining pressure of 40 MPa in saturated conditions. Red, green, and blue dots represent the cubic sample measurements obtained at atmospheric pressure for *x*, *y*, and *z* directions, respectively. The dashed sections indicate regions beyond the constraint proposed by Kuster and Toksöz (1974).

spectra as well as micro-crack closure, we constructed velocity-porosity relationships as a function of confining pressure. This pressure-dependence on velocity is important when constructing in-situ velocity-porosity relationships and applying them to seismic data. The velocity-porosity relationship that takes into account aspect ratio spectra is consistent with observations on over 100 cubic samples measured at atmospheric pressure, and generally shows pressure-dependent relationships between velocity and porosity. The agreement between theoretical relationships and laboratory data demonstrates that velocity-porosity relationships are well described by crack features (i.e. crack aspect ratio spectrum) and crack closure.

Acknowledgments

We are grateful to IODP Expedition 301 scientists and crews, especially to Co-chief Scientists Andrew Fisher (University California, Santa Cruz) and Tetsuro Urabe (University Tokyo), Staff Scientist Adam Klaus (Texas A&M University), and Shipboard Scientists Anne Bartetzko (University Bremen), Shusaku Goto (Kyoto University), Michael Hutnak (University California, Santa Cruz), and Mark Nielsen (Oregon State University). We also thank two anonymous reviewers for their helpful comments and suggestions. Furthermore, we also thank Fumio Kono and Tatsuo Saeki (TRC, JOGMEC) for the measurement of velocities. This research used samples and data provided by the Integrated Ocean Drilling Program (IODP). The United States Science Support Program supported part of this research. This research was partly supported by the Japan Agency for Marine-Earth Science and Technology (JAMSTEC) and Japan Drilling Earth Science Consortium (J-DESC).

References

Alt, J. C., Honnorez, J., Laverne, C., and Emmermann, R., 1986, Hydrothermal alteration of a 1 km section through the upper oceanic crust, Deep Sea Drilling Project hole 504B: mineralogy, chemistry, and evolution of seawater-basalt interactions: *Journal of Geophysical Research* **91**, 10309–10335.

Berryman, J. G., 1980, Long-wavelength propagation in composite elastic media: *Journal of the Acoustical Society of America* **68**, 1809–1831. doi: 10.1121/1.385171

Berryman, J. G., and Berge, P. A., 1996, Critique of two explicit schemes for estimating elastic properties of multiphase composites: *Mechanics of Materials* **22**, 149–164. doi: 10.1016/0167-6636(95)00035-6

Biot, M. A., 1955, Theory of elasticity and consolidation for a porous anisotropic solid: *Journal of Applied Physics* **26**, 115–135.

Birch, F., 1960, The velocity of compressional waves in rocks to 10 kilobars: *Journal of Geophysical Research* **65**, 1083–1102.

Cerney, B., and Carlson, R. L., 1999, The effect of cracks on the seismic velocities of basalt from site 990, southeast Greenland margin, in H. C Larsen, R. A. Duncan, J. F. Allan, and K. Brooks, eds. *Proceedings of the Ocean Drilling Program, Scientific Results* **163**: College Station, TX (Ocean Drilling Program), 29–35.

Cheng, C. H., and Toksöz, M. N., 1979, Inversion of seismic velocities for the pore aspect ratio spectrum of a rock: *Journal of Geophysical Research* **84**, 7533–7543.

Davis, E. E., and Currie, R. G., 1993, Geophysical observations of the northern Juan de Fuca Ridge system: lessons in sea-floor spreading: *Canadian Journal of Earth Sciences* **30**, 278–300.

Expedition 301 Scientists, 2005, Site U1301, in A. T. Fisher, T. Urabe, A. Klaus, and the Expedition 301 Scientists, *Proceedings of the Integrated Ocean Drilling Program* **301**, 2005: College Station TX (Integrated Ocean Drilling Program Management International, Inc.), doi: 10.2204/iodp.proc.301.106

Fisher, A. T., Becker, K., and Davis, E. E., 1997, The permeability of young oceanic crust east of Juan de Fuca Ridge determined using borehole thermal measurements: *Geophysical Research Letters* **24**, 1311–1314. doi: 10.1029/97GL01286

Fisher, A. T, and Davis, E. E., 2000, An introduction to the scientific results of Leg 168, in A. T. Fisher, E. E. Davis, and C. Escutia, eds, *Proceedings of the Ocean Drilling Program, Scientific Results*, **168**, College Station TX (Ocean Drilling Program), 3–5.

Fisher, A. T., Urabe, T., and Klaus, A., and the Expedition 301 Scientists, 2005, Integrated Ocean Drilling Program, U.S. Implementing Organization Expedition 301, *Scientific Prospectus, The hydrogeologic architecture of basaltic oceanic crust: compartmentalization, anisotropy, microbiology, and crustal-scale properties on the eastern flank of Juan de Fuca Ridge*.

Johnston, D. H., Toksöz, M. N., and Timur, A., 1979, Attenuation of seismic waves in dry and saturated rocks. II. Mechanisms *Geophysics* **44**, 691–711. doi: 10.1190/1.1440970

Hudson, J. A., 1981, Wave speeds and attenuation of elastic waves in material containing cracks: *Geophysical Journal of the Royal Astronomical Society* **64**, 133–150.

Hyndman, R. D., 1979, Poisson's ratio in the oceanic crust: a review *Tectonophysics* **59**, 321–333. doi: 10.1016/0040-1951(79)90053-2

Knight, R., and Nolen-Hoeksema, R., 1990, A laboratory study of the dependence of elastic wave velocities on pore scale fluid distribution: *Geophysical Research Letters* **17**, 1529–1532.

Kuster, G. T., and Toksöz, M. N., 1974, Velocity and attenuation of seismic waves in two-phase media, Part 1. Theoretical formulations: *Geophysics* **39**, 587–606. doi: 10.1190/1.1440450

Ludwig, R. J., Iturrino, G. J., and Rona, P. A., 1998, Seismic velocity-porosity relationship of sulfide, sulfate, and basalt samples from the TAG hydrothermal mound, in P. M. Herzig, S. E. Humphris, D. J. Miller, R. A. Zierenberg, eds. *Proceedings of the Ocean Drilling Program, Scientific Results,* **158**: College Station, TX (Ocean Drilling Program), 313–327.

Mavko, G., Mukerji, T., and Dvorkin, J., 1998, *The Rock Physics Handbook, Tools for Seismic Analysis of Porous Media*, Cambridge University Press.

Shearer, P. M., 1988, Cracked media, Poisson's ratio and the structure of the upper oceanic crust: *Geophysical Journal* **92**, 357–362. doi: 10.1111/j.1365-246X.1988.tb01149.x

Swift, S. A., Lizarralde, D., Stephen, R. A., and Hoskins, H., 1998, Velocity structure in upper ocean crust at Hole 504B from vertical seismic profiles: *Journal of Geophysical Research* **103**, 15361–15376. doi: 10.1029/98JB00766

Toksöz, M. N., Cheng, C. H, and Timur, A., 1976, Velocity of seismic waves in porous rocks: *Geophysics* **41**, 621–645. doi: 10.1190/1.1440639

Toksöz, M. N., Johnston, D. H., and Timur, A., 1979, Attenuation of seismic waves in dry and saturated rocks. 1. Laboratory measurements: *Geophysics* **44**, 681–690. doi: 10.1190/1.1440969

Tompkins, M. J., and Christensen, N. L., 1999, Effect of pore pressure on compressional wave attenuation in a young oceanic basalt: *Geophysical Research Letters* **26**, 1321–1324. doi: 10.1029/1999GL900216

Tsuji, T., and Yamaguchi, H., 2007, Improvement of Mineral Mapping Method: Application of Neural Network System to Elemental Maps by Electron Microprobe Analyzer, *Proceedings of the 117th SEGJ Conference*, 1–4.

Walsh, J. B., 1966, Seismic attenuation in rock due to friction: *Journal of Geophysical Research* **71**, 2591–2599.

Wepfer, W. W., and Christensen, N. I., 1991, Q structure of the oceanic crust: *Marine Geophysical Researches* **99**, 3043–3056.

Wilkens, R. H., Christensen, and N. I., Slater, L., 1983, High-pressure seismic studies of Leg 69 and 70 basalts, in J. R. Cann, M. G. Langseth, J. Honnorez, R. P. Von Herzen, and S. M. White, et al., *Initial Reports of the Deep Sea Drilling Project* **69**, 683–686.

Wilkens, R. H., Schultz, D., and Carlson, R. L., 1988, Relationship of resistivity, velocity, and porosity for basalts from downhole well logging measurements in Hole 418A, in M. H. Salisbury and J.H. Scott, et al. *Proceedings of the Ocean Drilling Program, Scientific Results* **102**, 69–78.

Wilkens, R. H., Fryer, G. J., and Karsten, J., 1991, Evolution of porosity and seismic structure of upper oceanic crust: importance of aspect ratios: *Journal of Geophysical Research* **96**, 17891–17995.

Wilkens, R. H., and Salisbury, M. H., 1996, Microstructure and physical properties of samples from Hole 896A, in J. C. Alt, H. Kinoshita, L. B. Stokking, and P. J. Michael, et al. *Proceedings of the Ocean Drilling Program, Scientific Results* **148B**, 365–374.

Manuscript received 7 August 2007; accepted 14 December 2007.

Appendix: P-wave quality factor

Quality factor is another important acoustic property obtained from laboratory measurements and is closely related to crack intensity, mineral composition, and mineral textures (e.g. Johnston et al., 1979). P-wave quality factors (Figure A) were calculated from the stored signal waveforms (Figure 4) using a spectrum division technique (Toksöz et al., 1979). In order to ensure similar coupling and pressure conditions for both the sample and a reference standard, the signals from an aluminum cylinder of the same sample size were recorded at various pressure steps and used as reference signals. Measurements were carried out in both saturated and dry conditions. The calculated quality factors are affected by many attenuation mechanisms (e.g. matrix inelasticity, viscosity and flow of saturating fluids, and scattering from inclusions), and we cannot fully account for each attenuation mechanism.

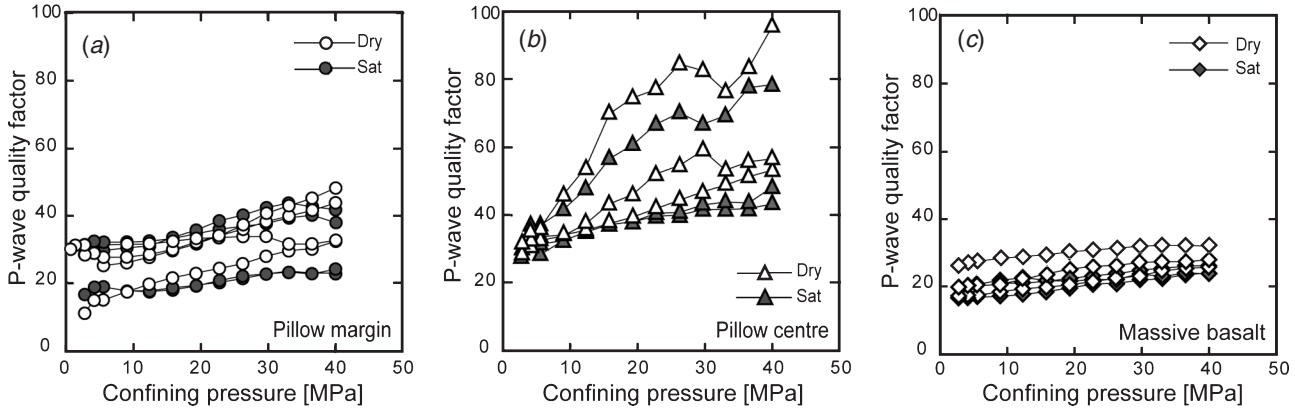

Fig. A: P-wave quality factors as a function of confining pressure in (*a*) the pillow margins, (*b*) the centre parts of pillow basalts, and (*c*) the massive basalts. Open and solid symbols represent quality factors in dry and saturated conditions, respectively.

The P-wave quality factors increase with confining pressure, mainly due to closure of micro-cracks, and the trend suggests that values would increase further beyond the maximum pressure (40 MPa) used in the experiment. As a result of micro-crack closure with increasing confining pressure, the frictional dissipation due to relative motions at the grain boundaries and across crack surfaces (Walsh, 1966) becomes small. Furthermore, most P-wave quality factors measured in saturated basaltic samples are lower than those of dry samples (Figure A) because the fluid-associated attenuation is not considered when dealing with dry conditions (e.g. Johnston et al., 1979).

We can find a clear relationship between quality factor and porosity (Figure B-*a*), similar to that previously reported by Wepfer and Christensen (1991) where quality factor increases rapidly with decreasing porosity. The high quality factor near zero porosity may indicate that the grain mineral inelasticity is very low. In addition, quality factor-velocity relationships (Figure B-*c*) clearly show that P-wave quality factors increase rapidly (nonlinearly) with velocities.

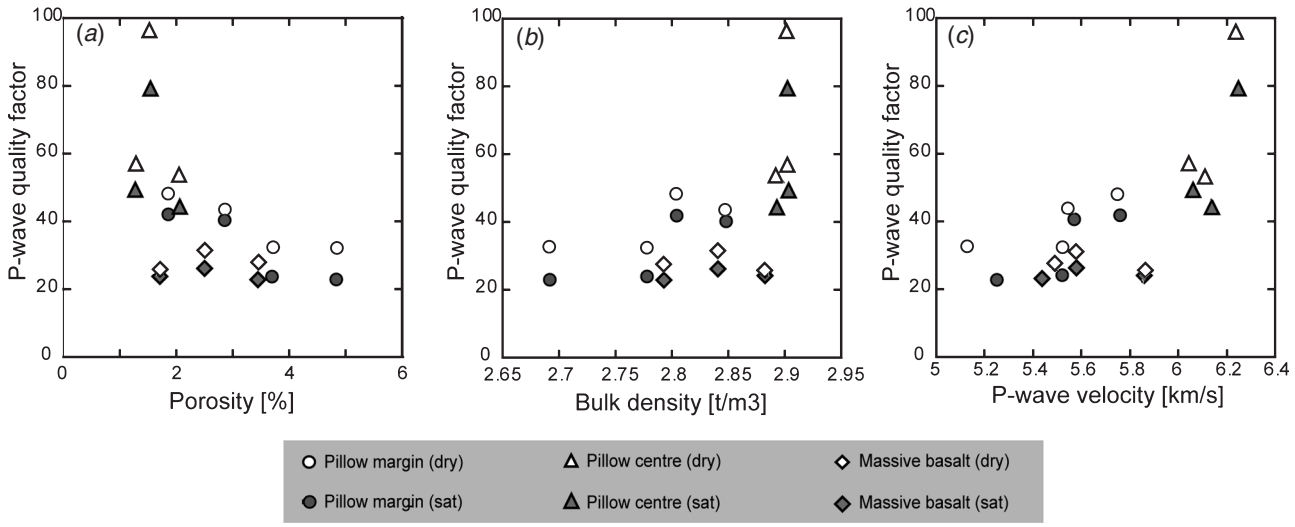

Fig. B: Diagrams showing relationships (*a*) between P-wave quality factor and porosity, (*b*) between P-wave quality factor and bulk density, and (*c*) between P-wave quality factor and P-wave velocity. Quality factors represented in this figure were calculated from the waveforms obtained at a confining pressure of 40 MPa. Open and solid symbols represent the measurements obtained in dry and saturated conditions, respectively.

As in the case of the velocities, P-wave quality factors for centre parts of pillow basalts are higher than those obtained from the pillow margins (Figure A), whereas P-wave quality factors of the massive basalts are lower than those of the pillow basalts. The relationship between quality factors and porosities (Figure B) further demonstrate that the massive basalts have low quality factors, compared

to pillow basalts with similar porosities. One possible explanation for this is that significant scattering occurs at the 1 MHz source frequency (e.g. Johnston et al., 1979; Hudson, 1981) because of the relatively larger grain sizes in the groundmass of the massive basalts (Tsuji and Yamaguchi, 2007).

P-wave quality factors have an average value of ~31 at a confining pressure of 5.5 MPa, which corresponds to in situ effective pressure. Tompkins and Christensen (1999) reported that P-wave quality factors of the dredged samples of Juan de Fuca Ridge are 11–17 at hydrostatic pore pressure. The discrepancy in P-wave quality factors between the two studies could be attributed to the fact that the samples from the Tompkins and Christensen (1999) study were obtained from seafloor dredges, whereas the samples used in this study were obtained at 100 km off axis of the Juan de Fuca Ridge and in situ below an ~265 m thick sedimentary cover. Furthermore, the difference may represent lateral variations away from ridge crests and different degrees of alteration associated with water-rock interactions at their respective locations. In addition, quality factor measurements are highly dependent on several parameters including strain amplitude (Johnston et al., 1979) as well as the measurement technique; when comparing to the quality factor of low-frequency seismic data, we also need to consider the scale (source frequency) differences. Therefore, it is difficult to compare results from different studies in a quantitatively manner.

ファンデフーカ海嶺東翼部海洋性玄武岩の有効圧下における弾性波速度と間隙率の関係：クラック閉鎖が弾性波速度に与える影響

辻　健[1]・ジェラルド J. イットゥリーノ[2]

要　旨：　ファンデフーカ(Juan de Fuca)海嶺東翼部から取得された海洋性玄武岩サンプルの弾性波速度を有効圧下で測定し，クラックの形状･有効圧に伴う開口クラックの減少から有効圧に依存した弾性波速度と間隙率の関係を構築することを試みた。まず，有効圧に伴う弾性波速度の増加は開口クラックの減少によって生じるとし，玄武岩サンプル内のマイクロクラックのアスペクト比分布を Kuster- Toksöz 理論を用いて推定した。その結果，本研究で測定した 10 個の玄武岩サンプルでは，マイクロクラックのアスペクト比分布は同様の特徴を持つことが分かった。そこで，推定したマイクロクラックのアスペクト比分布を間隙率で規格化し，各間隙率に対応したアスペクト比分布を求めることで，弾性波速度と間隙率の関係を理論的に計算した。さらに，有効圧に伴う開口クラックの減少を考慮することで，有効圧に依存した弾性波速度と間隙率の関係を構築した。その関係は,同じ掘削孔から得られた他の玄武岩サンプルの測定値と,間隙率の広い範囲において整合的であることが認められた。その整合性から，海洋性玄武岩の弾性波速度と間隙率の関係及びその有効圧依存性は，クラックの形状（アスペクト比分布）と有効圧に伴う開口クラックの減少によって表現できることが示された。

キーワード：弾性波速度と間隙率の関係，クラックの形状，海洋性玄武岩，Kuster-Toksöz 理論，統合国際掘削計画

Juan de Fuca 해저산맥의 동쪽 측면으로부터 얻은 해양성 현무암의 속도와 공극률의 관계: 균열닫힘이 탄성파 속도에 미치는 영향

Takeshi Tsuji[1] and Gerardo J. Iturrino[2]

요 약：　해양성 현무암층에 대해 현장에서의 속도와 공극률의 관계를 알기 위해서 Juan de Fuca 해저산맥의 동쪽 측면으로부터 채취한 현무암 시료들에 대해 최고 40MPa 구속압력(confining pressure)하에서 균열 특성을 고려하며 P파와 S파 속도를 측정하였다. 구속압력에 따른 속도의 변화는 미세균열의 닫힘(microcrack closure)에 기인한다고 가정하고, Kuster-Toksöz 이론을 이용하여 미세균열의 개구비 스펙트라(micro-crack aspect ratio spectra)를 측정하였다. 그 결과 서로 다른 시료들의 정규화된 개구비 스펙트라들이 유사한 특성을 갖는다는 것을 보여주었다. 그리고 나서 정규화된 개구비 스펙트럼(spectrum)으로부터, 각 공극률에 대한 개구비 스펙트럼을 계산함으로써 이론적인 속도와 공극률의 관계를 만들었다. 또한 구속압력에 따른 미세균열 닫힘을 고려하여 구속압력의 함수로서의 속도-공극률 관계를 얻을 수 있었다. 개구비 스펙트라를 고려한 이론적인 관계는 대기압하에서 측정된 100개가 넘는 시료들에 대해 관찰된 관계와 잘 일치하고, 넓은 범의의 공극률에 대해 일반적으로 관찰되는 압력 의존적인 관계와도 잘 일치된다. 실험에서 유도된 자료들과 이론적으로 계산된 값들의 일치를 통해 Juan de Fuca 해저산맥의 동쪽 측면으로부터 얻어진 현무암 시료의 속도와 공극률의 관계는 군열의 특성(즉, 정규화된 개구비 스펙트라)과 균열 담힘에 의해 설명되어질 수 있음을 알 수 있다.

주요어：속도와 공극률 관계, 해양 현무암, 균열 개구비, Kuster-Toksöz 이론,
통합해양시추 프로그램 (integrated ocean drilling program)

1 京都大学大学院　工学研究科 社会基盤工学専攻
〒615-8540　京都市西京区京都大学桂 C1-1-110
2 コロンビア大学　ラモント・ドハティ地球物理学研究所

1 교토 대학, 공학 연구과 사회기반공학전공
2 미국 콜럼비아 대학, Lamont-Doherty Earth Observatory